ΣIGMA: Scale-Invariant Global Sparse Shape Matching Supplementary

A. Proofs

In the following we provide proofs for all lemmata from the main paper.

A.1. Proof of Lemma 1

Invariance of the PLBO We demonstrate that, despite using the vertex coordinates $\mathbf{X}$ explicitly, the operator $\Delta^{(\mathcal{X})}_{\text{proj}}$ is agnostic to the extrinsic orientation of the input pose $\mathcal{X}$. Specifically, it is invariant under arbitrary rigid body transformations from the Euclidean group $\mathrm{E}(3)$.

Lemma 1. *Let $\Delta(\mathbf{X}) := \Delta^{(\mathcal{X})}_{\text{proj}} \in \mathbb{R}^{|\mathbf{X}|\times|\mathbf{X}|}$ be the projected Laplace-Beltrami operator for the vertices $\mathbf{X}$, defined in Eqn. (1). For any rigid body transformation*

$$\begin{pmatrix} \mathbf{R} & \mathbf{t} \\ \mathbf{0} & 1 \end{pmatrix} \in \mathrm{E}(3), \quad \textit{with } \mathbf{R} \in \mathrm{O}(3), \mathbf{t} \in \mathbb{R}^3, \tag{10}$$

it holds that $\Delta(\mathbf{X}) = \Delta(\mathbf{X}\mathbf{R}^\top + \mathbf{1}\mathbf{t}^\top)$.

Proof. We first simplify the rigidly transformed vertices $\mathbf{X}\mathbf{R}^\top + \mathbf{1}\mathbf{t}^\top$ in homogeneous coordinates

$$\begin{pmatrix} \mathbf{X}\mathbf{R}^\top + \mathbf{1}\mathbf{t}^\top & \mathbf{1} \end{pmatrix} = \begin{pmatrix} \mathbf{X} & \mathbf{1} \end{pmatrix} \begin{pmatrix} \mathbf{R}^\top & \mathbf{0} \\ \mathbf{t}^\top & 1 \end{pmatrix} = \tilde{\mathbf{X}}\mathbf{Q}^\top \tag{11}$$

where $\tilde{\mathbf{X}} := \begin{pmatrix} \mathbf{X} & \mathbf{1} \end{pmatrix} \in \mathbb{R}^{|\mathbf{X}|\times 4}$ is the neutral input pose and $\mathbf{Q} := \begin{pmatrix} \mathbf{R} & \mathbf{t} \\ \mathbf{0} & 1 \end{pmatrix}$. We then directly obtain the invariance of the projection matrix defined in Eqn. (2)

$$\begin{aligned} \mathbf{\Pi}_{\mathbf{X}\mathbf{R}^\top + \mathbf{1}\mathbf{t}^\top} &= \mathbf{I} - \tilde{\mathbf{X}}\mathbf{Q}^\top (\mathbf{Q}\tilde{\mathbf{X}}^\top \tilde{\mathbf{X}}\mathbf{Q}^\top)^{-1}\mathbf{Q}\mathbf{X}^\top \\ &= \mathbf{I} - \tilde{\mathbf{X}}(\tilde{\mathbf{X}}^\top\tilde{\mathbf{X}})^{-1}\tilde{\mathbf{X}}^\top = \mathbf{\Pi}_{\mathbf{X}}. \end{aligned} \tag{12}$$

The last equality is valid for any $\mathbf{Q}$, because $\mathrm{E}(3) \subset \mathrm{GL}(4)$. Since the Laplacian matrix $\Delta^{(\mathcal{X})}_{\text{stiff}}$ is, by construction, invariant under rigid-body transformations, inserting Eqn. (12) into Eqn. (1) directly yields the desired equality. □

A.2. Proof of Lemma 2

Lemma 2. *Let $\left(\mathbf{P}, \hat{\mathbf{X}}, \hat{\mathbf{Y}}\right)$ be a global optimiser of Eqn. (4).*

(a) Let $\mathcal{X}' := \left(s\mathbf{X}, \mathbf{F}^{(\mathcal{X})}, \mathcal{I}\right)$ be a rescaled input shape $\mathcal{X}$, where a scalar factor $s > 0$ is applied to the vertex coordinates. Then $\left(\mathbf{P}', \hat{\mathbf{X}}', \hat{\mathbf{Y}}'\right) := \left(\mathbf{P}, \hat{\mathbf{X}}, s\hat{\mathbf{Y}}\right)$ is a global optimiser of Eqn. (4) between $\mathcal{X}'$ and $\mathcal{Y}$.

(b) Let $\mathcal{X}'' := \left(\mathbf{X}\mathbf{R}^\top + \mathbf{1}\mathbf{t}^\top, \mathbf{F}^{(\mathcal{X})}, \mathcal{I}\right)$ be a rigidly transformed version of $\mathcal{X}$ with $\mathbf{R} \in \mathrm{SO}(3), \mathbf{t} \in \mathbb{R}^3$. Then $\left(\mathbf{P}'', \hat{\mathbf{X}}'', \hat{\mathbf{Y}}''\right) := \left(\mathbf{P}, \hat{\mathbf{X}}, \hat{\mathbf{Y}}\mathbf{R}^\top + \mathbf{1}\mathbf{t}^\top\right)$ is a global optimiser of Eqn. (4) between $\mathcal{X}''$ and $\mathcal{Y}$.

Lemma 2a – Invariance of Global Scaling

Proof. Rescaling the shape $\mathcal{X} \to \mathcal{X}'$ affects the shape diameter in the same manner $d'_{\mathcal{X}} = s\, d_{\mathcal{X}}$ with $s > 0$. On the other hand, the orientation features $\mathbf{h}^\bullet$ are fully scale invariant, since we leverage scale-invariant scalar input fields and the outer normals are normalised to unit length. Likewise, the Laplacian stiffness matrix $\Delta^{(\mathcal{X})}_{\text{stiff}}$ is unaffected, and the projection $\mathbf{\Pi}^{(\mathcal{X})}$ defined in Eqn. (2) of $\mathcal{X}'$ becomes:

$$\begin{aligned} \mathbf{\Pi}^{(\mathcal{X}')} &= \mathbf{I} - \tilde{\mathbf{X}}\mathbf{S}\big((\tilde{\mathbf{X}}\mathbf{S})^\top \tilde{\mathbf{X}}\mathbf{S}\big)^{-1}(\tilde{\mathbf{X}}\mathbf{S})^\top \\ &= \mathbf{I} - \tilde{\mathbf{X}}(\tilde{\mathbf{X}}^\top\tilde{\mathbf{X}})^{-1}\tilde{\mathbf{X}}^\top = \mathbf{\Pi}^{(\mathcal{X})}, \end{aligned} \tag{13}$$

where the homogeneous coordinates $\tilde{\mathbf{X}}$ are rescaled with the diagonal matrix $\mathbf{S} := \mathrm{diag}(s, s, s, 1) \in \mathbb{R}^{4\times 4}$. Hence, the projected LBO $\Delta^{(\mathcal{X})}_{\text{proj}}$ from Eqn. (1) scale-invariant.

Inserting these scale shift identities yields the following optimisation problem Eqn. (14):

$$\begin{aligned} \min_{\mathbf{P}', \hat{\mathbf{X}}', \hat{\mathbf{Y}}'} \quad & \frac{1}{nd_{\mathcal{Y}}}\left\|\hat{\mathbf{X}}'_{\mathcal{I}} - \mathbf{P}'\mathbf{Y}_{\mathcal{J}}\right\|_F + \frac{1}{nd_{\mathcal{X}}}\left\|\frac{1}{s}\hat{\mathbf{Y}}'_{\mathcal{J}} - \mathbf{P}'^\top\mathbf{X}_{\mathcal{I}}\right\|_F \\ & + \frac{\lambda_{\text{def}}}{|\mathbf{X}|d_{\mathcal{Y}}}\left\|\Delta^{(\mathcal{X})}_{\text{proj}}\hat{\mathbf{X}}'\right\|_F + \frac{\lambda_{\text{def}}}{|\mathbf{Y}|d_{\mathcal{X}}}\left\|\frac{1}{s}\Delta^{(\mathcal{Y})}_{\text{proj}}\hat{\mathbf{Y}}'\right\|_F \\ & + \frac{\lambda_{\text{ori}}}{n}\left\|\mathbf{h}^{(\mathcal{X})} - \mathbf{P}'\mathbf{h}^{(\mathcal{Y})}\right\|_F, \\ \text{s.t.} \quad & \mathbf{P}' \in \{0,1\}^{n\times n},\ \mathbf{P}'^\top\mathbf{1}_n = \mathbf{1}_n,\ \mathbf{P}'\mathbf{1}_n = \mathbf{1}_n, \end{aligned} \tag{14}$$

Substituting $\mathbf{P}' \to \mathbf{P}$, $\hat{\mathbf{X}}' \to \hat{\mathbf{X}}$ and $\frac{1}{s}\hat{\mathbf{Y}}' \to \hat{\mathbf{Y}}$ then results in exactly the optimisation problem from Eqn. (4) with the original inputs $\mathcal{X}$ and $\mathcal{Y}$. Inserting the global optimiser from

the original, unscaled problem $\left(\mathbf{P}, \hat{\mathbf{X}}, \hat{\mathbf{Y}}\right)$ directly results in the global optimiser $\left(\mathbf{P}', \hat{\mathbf{X}}', \hat{\mathbf{Y}}'\right) = \left(\mathbf{P}, \hat{\mathbf{X}}, s\hat{\mathbf{Y}}\right)$ of the scaled problem. □

Lemma 2b – Invariance of Rigid Transformations

Proof. Applying a rigid transformation $\mathcal{X} \rightarrow \mathcal{X}''$ to the shape $\mathbf{X} \rightarrow \mathbf{X}\mathbf{R}^\top + \mathbf{1}\mathbf{t}^\top$ leads to $\mathbf{X}_\mathcal{I} \rightarrow \mathbf{X}_\mathcal{I}\mathbf{R}^\top + \mathbf{1}\mathbf{t}^\top$ directly, where $\mathbf{R} \in \mathrm{SO}(3)$ and $\mathbf{t} \in \mathbb{R}^3$. On the other hand, $\Delta^{(\mathcal{X})}_{\text{proj}}$ is invariant to rigid transformation (cf. Lemma 1), so the term $\Delta^{(\mathcal{X})}_{\text{proj}}$ stays unaffected. Furthermore, the orientation-aware features $\mathbf{h}^\bullet$ are rigid transformation invariant, as discussed in Sec. 3.2 of the main paper.

Inserting these rigid transformation identities yields the following optimisation problem Eqn. (15):

$$\begin{aligned}
\min_{\mathbf{P}'', \hat{\mathbf{X}}'', \hat{\mathbf{Y}}''} \quad & \frac{1}{nd_\mathcal{Y}} \left\| \hat{\mathbf{X}}''_\mathcal{I} - \mathbf{P}''\mathbf{Y}_\mathcal{J} \right\|_F \\
& + \frac{1}{nd_\mathcal{X}} \left\| \hat{\mathbf{Y}}''_\mathcal{J} - \mathbf{P}''^\top(\mathbf{X}_\mathcal{I}\mathbf{R}^\top + \mathbf{1}\mathbf{t}^\top) \right\|_F \\
& + \frac{\lambda_{\text{deform}}}{|\mathbf{X}|d_\mathcal{Y}} \left\| \Delta^{(\mathcal{X})}_{\text{proj}} \hat{\mathbf{X}}'' \right\|_F + \frac{\lambda_{\text{deform}}}{|\mathbf{Y}|d_\mathcal{X}} \left\| \Delta^{(\mathcal{Y})}_{\text{proj}} \hat{\mathbf{Y}}'' \right\|_F \\
& + \frac{\lambda_{\text{orient}}}{n} \left\| \mathbf{h}^{(\mathcal{X})} - \mathbf{P}''\mathbf{h}^{(\mathcal{Y})} \right\|_F, \qquad (15) \\
\text{s.t.} \quad & \mathbf{P}'' \in \{0,1\}^{n \times n},\ \mathbf{P}''^\top \mathbf{1}_n = \mathbf{1}_n,\ \mathbf{P}''\mathbf{1}_n = \mathbf{1}_n,
\end{aligned}$$

Substituting $\mathbf{P}'' \rightarrow \mathbf{P}$, $\hat{\mathbf{X}}'' \rightarrow \hat{\mathbf{X}}$ and $\hat{\mathbf{Y}}'' \rightarrow \hat{\mathbf{Y}}\mathbf{R}^\top + \mathbf{1}\mathbf{t}^\top$, we have:

$$\begin{aligned}
\min_{\mathbf{P}, \hat{\mathbf{X}}, \hat{\mathbf{Y}}} \quad & \frac{1}{nd_\mathcal{Y}} \left\| \hat{\mathbf{X}}_\mathcal{I} - \mathbf{P}\mathbf{Y}_\mathcal{J} \right\|_F \\
& + \frac{1}{nd_\mathcal{X}} \left\| (\hat{\mathbf{Y}}_\mathcal{J}\mathbf{R}^\top + \mathbf{1}\mathbf{t}^\top) - \mathbf{P}^\top(\mathbf{X}_\mathcal{I}\mathbf{R}^\top + \mathbf{1}\mathbf{t}^\top) \right\|_F \\
& + \frac{\lambda_{\text{deform}}}{|\mathbf{X}|d_\mathcal{Y}} \left\| \Delta^{(\mathcal{X})}_{\text{proj}} \hat{\mathbf{X}} \right\|_F \\
& + \frac{\lambda_{\text{deform}}}{|\mathbf{Y}|d_\mathcal{X}} \left\| \Delta^{(\mathcal{Y})}_{\text{proj}} (\hat{\mathbf{Y}}\mathbf{R}^\top + \mathbf{1}\mathbf{t}^\top) \right\|_F \\
& + \frac{\lambda_{\text{orient}}}{n} \left\| \mathbf{h}^{(\mathcal{X})} - \mathbf{P}\mathbf{h}^{(\mathcal{Y})} \right\|_F, \qquad (16) \\
\text{s.t.} \quad & \mathbf{P} \in \{0,1\}^{n \times n},\ \mathbf{P}^\top \mathbf{1}_n = \mathbf{1}_n,\ \mathbf{P}\mathbf{1}_n = \mathbf{1}_n,
\end{aligned}$$

The first, third and fifth term in Eqn. (16) are same as the corresponding terms in the original problem of Eqn. (4), hence the only critical terms are the second and forth. The second can be rewritten as follows:

$$\begin{aligned}
& \left\| \hat{\mathbf{Y}}\mathbf{R}^\top + \mathbf{1}\mathbf{t}^\top - \mathbf{P}^\top(\mathbf{X}_\mathcal{I}\mathbf{R}^\top + \mathbf{1}\mathbf{t}^\top) \right\|_F \\
= & \left\| (\hat{\mathbf{Y}} - \mathbf{P}^\top\mathbf{X}_\mathcal{I})\mathbf{R}^\top \right\|_F \\
= & \left\| \hat{\mathbf{Y}} - \mathbf{P}^\top\mathbf{X}_\mathcal{I} \right\|_F \qquad (17)
\end{aligned}$$

The first equality holds because $\mathbf{P}^\top\mathbf{1} = \mathbf{1}$ holds by construction. The second equality follows from the fact the $\mathrm{SO}(3)$ elements do not affect the Frobenius norm.

For the forth term we have the following equalities:

$$\begin{aligned}
& \left\| \Delta^{(\mathcal{Y})}_{\text{proj}} (\hat{\mathbf{Y}}\mathbf{R}^\top + \mathbf{1}\mathbf{t}^\top) \right\|_F \\
= & \left\| \Delta^{(\mathcal{Y})}_{\text{proj}} \hat{\mathbf{Y}}\mathbf{R}^\top + \Delta^{(\mathcal{Y})}_{\text{proj}} \mathbf{1}\mathbf{t}^\top \right\|_F \\
= & \left\| \Delta^{(\mathcal{Y})}_{\text{proj}} \hat{\mathbf{Y}}\mathbf{R}^\top \right\|_F \\
= & \left\| \Delta^{(\mathcal{Y})}_{\text{proj}} \hat{\mathbf{Y}} \right\|_F \qquad (18)
\end{aligned}$$

where we utilise the linearity of the PLBO, and the fact that the constant vector $\mathbf{1}\mathbf{t}^\top$ lives in its nullspace (the first and second equality). The third equality holds because rotations do not affect the Frobenius norm.

Hence, $\left(\mathbf{P}'', \hat{\mathbf{X}}'', \hat{\mathbf{Y}}''\right) = \left(\mathbf{P}, \hat{\mathbf{X}}, \hat{\mathbf{Y}}\mathbf{R}^\top + \mathbf{1}\mathbf{t}^\top\right)$ is the global optimiser of the rigidly transformed problem. □

B. Implementation Details

B.1. Shape Reconstruction

In Fig. 3 examples of the reconstructed shapes using the area-normalised LBO, *i.e.* the stiffness matrix component $\Delta^{(\mathcal{X})}_{\text{stiff}}$ of the Laplacian, and PLBO are illustrated for qualitative comparison. It demonstrates that the PLBO leads to more realistic results whereas the LBO leads to oversmoothed reconstructions. For obtain these results, we fixed the correspondences in the $\mathcal{E}_{\text{rec}}$ term of our final objective defined in Eqn. (4) and run our full implementation to estimate $\hat{\mathbf{X}}$ and $\hat{\mathbf{Y}}$. This results in fast optimisation since the unknowns are continuous variables living in $\mathbb{R}^3$ and helps to show the quality of the reconstruction in very high resolution (10k faces) with clean correspondences. Since the reconstructed shapes are only a by-product of our method, we use lower resolution meshes (500 faces) in all experiments for the sake of faster optimisation, but a similar reconstruction behaviour of PLBO and LBO can be observed in this case as well.

The idea of projecting LBO has been explored in [26], with a focus on *preserving* a certain subspace of the LBO (approximating the low frequency end of the spectrum), for the task of fast spectral decomposition. In contrary, we aim to *exclude* the subspace of shape coordinates by the adding it to the kernel (of PLBO) for geometry reconstruction. Hence both approaches can be seen complementary.

B.2. Details on the Orientation-Aware Feature

Inspired by [33], the orientation-aware feature defined in Eqn. (8) requires two scalar-valued features $\mathbf{f}^{(\mathcal{X})}$ and $\mathbf{g}^{(\mathcal{X})}$ besides the unit outer normal $\mathbf{n}^{(\mathcal{X})}$ as input which encode the information of shape orientation. In theory, we can use any pair of scalar-valued features to construct an

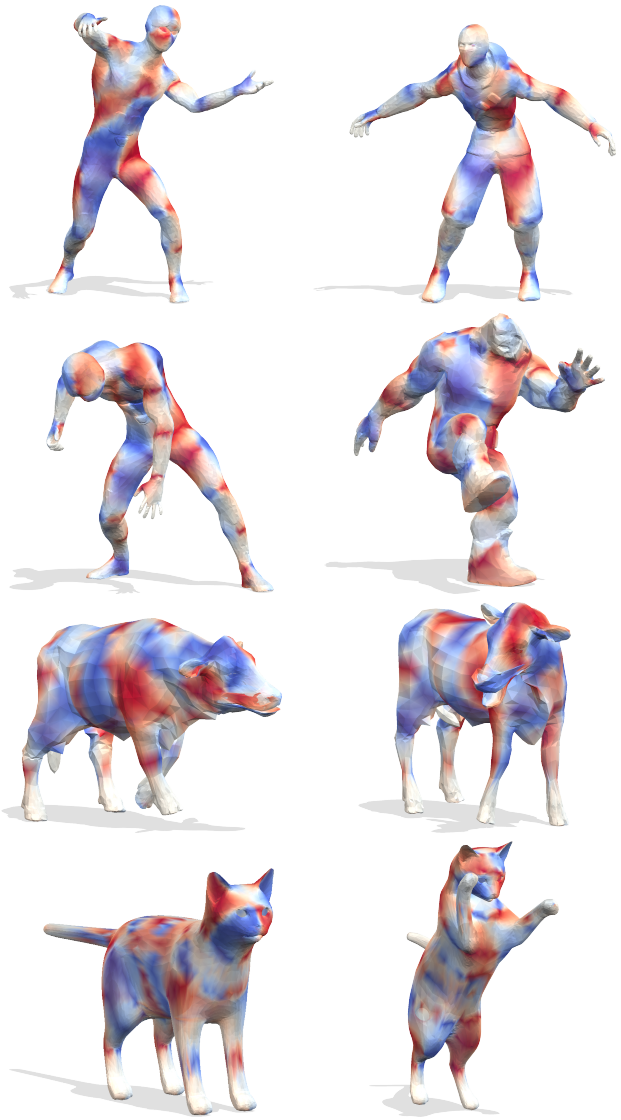

Figure 10: Visualisation of our **orientation-aware feature**. Red and blue indicate the respective orientation $-1, 1$ while white indicates values in-between.

orientation-aware feature map. However, there are several aspects one needs to take into consideration. First, the scalar-values features should be scale invariant. Second, their gradient fields should not be close to parallel, since the cross-product of two parallel vectors will vanish. In practice, we choose the 1st and 70-th frequency of the wave kernel signature [4] as the $\mathbf{f}^{(\mathcal{X})}$ and $\mathbf{g}^{(\mathcal{X})}$ due to their dissimilar frequencies which effectively avoids near-parallel gradient fields. Empirically we found it works well for our purpose. See Fig. 10 for an illustration. Note that although the orientation-aware features can be easily computed densely for every vertex, only the ones for the sparse keypoints are

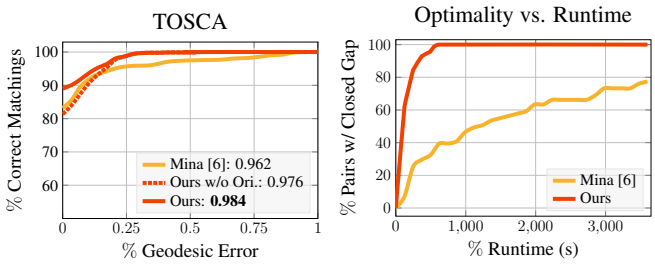

Figure 11: Quantitative results with $k = 5$ for MINA [6] and ours. Our method produces global optimal results for **all** instances for this (smaller) optimisation problem within 15min.

utilised in Eqn. (7). As shown in Fig. 10, the feature map is noisy, especially under the presence of non-isometric deformations. Hence, it helps to disambiguate the intrinsic shape symmetry, however, it does not fully exclude symmetrically flipped matchings and does not lead to fine-grain feature alignment.

C. Further Experiments

C.1. Experiments with Default Settings in MINA [6]

The results shown in the main paper are obtained under a more conservative search space pruning than was proposed in the original paper, namely $k = 11$, where the original MINA defaults to $k = 5$. Below we show additional experimental results using $k = 5$ and argue that in general less pruning is more favourable.

As shown in Fig. 11, MINA achieves accurate correspondences and certifies 80% globally optimal pairs within 1h in its original setting with a solution search space restricted to only allowing $k = 5$ matching candidates per keypoint. In this setting, SIGMA still outperforms MINA and is able to find the global optima of all 71 TOSCA [9] matching pairs with better accuracy within 15 minutes. Note that the matching accuracy of SIGMA does not improve compared to the case of $k = 11$ (cf. Fig. 4), this is because the more aggressive pruning inevitably excludes some correct matchings which effects the matching performance negatively. Therefore, a more conservative pruning with higher k is preferable in practice. Removing the pruning completely leads to an extremely enlarged search space and, thus, also higher runtime.

C.2. Robustness to Keypoints

Compared to MINA, our SIGMA is less sensitive to the exact position of keypoints. Our experiments (Fig. 4, 6) on SHREC20 non-isometric shows the robustness of SIGMA, since the keypoints were hand-picked by the dataset author and an absolute matching does not exist. Addition-

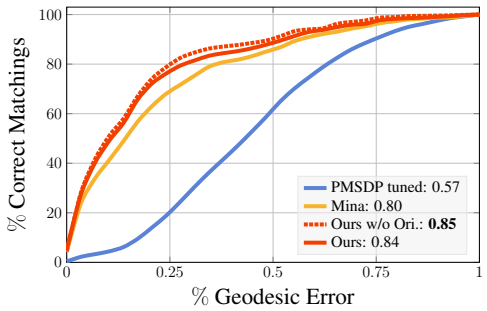

Figure 12: PCK curves on SMAL [51] with independent FPS Sampling.

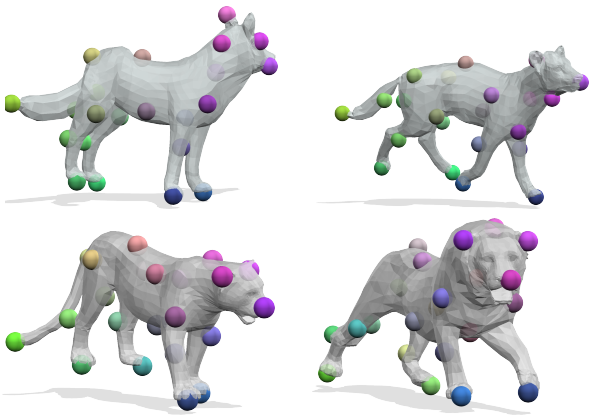

Figure 13: Qualitative results of SIGMA on SMAL [51] with independently FPS-sampled keyponits.

ally we consider the challenging scenario of sampling the keypoints for each shape independently using farthest point sampling (FPS). Here, there are no guarantees that meaningful correspondences exist. Quantitative and qualitative results on SMAL can be seen in Fig. 12, 13. Compared to other keypoint-dependent approaches (MINA and PMSDP), our method is the least sensitive to keypoint positions but a certain drop in performance is expected.

C.3. Ablation on λ_{rec} & λ'_{ori}

Our ablation is based on 20 randomly sampled TOSCA shape pairs and an (equivalent) version of the original objective presented in Eq. (4) for practical reasons.

$$\lambda_{\text{rec}}\mathcal{E}_{\text{rec}}(\mathbf{P},\hat{\mathbf{X}},\hat{\mathbf{Y}}) + \mathcal{E}_{\text{def}}(\hat{\mathbf{X}},\hat{\mathbf{Y}}) + \lambda'_{\text{ori}}\mathcal{E}_{\text{ori}}(\mathbf{P}) \quad (19)$$

We note it can be easily converted to the formulation in Eq. (4) by setting $\lambda_{\text{rec}} = \lambda_{\text{def}}^{-1}$ and $\lambda'_{\text{ori}} = \lambda_{\text{ori}} * \lambda_{\text{rec}}$. Moreover, all the experiments (except otherwise mentioned) are conducted under the setting of $\lambda_{\text{def}} = 5$ and $\lambda_{\text{ori}} = 2.5\text{e}{-2}$, which corresponds to $\lambda_{\text{rec}} = 2\text{e}{-1},\ \lambda'_{\text{ori}} = 5\text{e}{-3}$.

As both the $\mathcal{E}_{\text{rec}}$ and $\mathcal{E}_{\text{def}}$ terms in the objective are dispensable (cf. Eq. (4, 19)), we first conduct the ablation on λ_{rec} alone, i.e. $\lambda'_{\text{ori}} = 0$. The search range covers from $1\text{e}{-8}$ to $1\text{e}5$ in logarithmic scale, with a refined search range between $1\text{e}{-1}$ and $1\text{e}0$. As shown in Fig. 14 (left), the set of minimal mean geodesic error are achieved at $\{1\text{e}{-5},\ 3\text{e}{-1},\ 9\text{e}{-1}\}$.

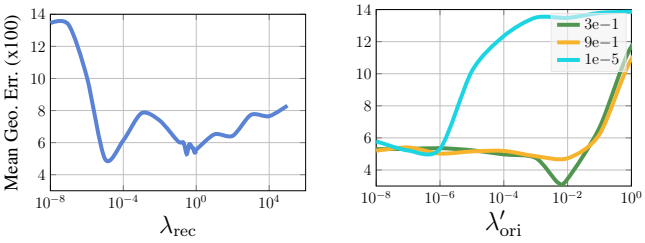

Figure 14: **Ablation study** on λ_{rec} & λ'_{ori}. (Left) By setting $\lambda'_{\text{ori}} = 0$, the lowest mean geodesic errors are obtained at $\lambda_{\text{rec}} \in \{1\text{e}{-5},\ 3\text{e}{-1},\ 9\text{e}{-1}\}$ (Right) The λ_{rec} is fixed to be $\{1\text{e}{-5},\ 3\text{e}{-1},\ 9\text{e}{-1}\}$ respectively, the lowest mean geodesic error is obtained at $\lambda'_{\text{ori}} = 5\text{e}{-3}$. Note that overall the (cyan) curve with $\lambda_{\text{rec}} = 1\text{e}{-5}$ lies above the other two curves, suggesting its suboptimal performance.

Consequently, we fix λ_{rec} to be $\{1\text{e}{-5},\ 3\text{e}{-1},\ 9\text{e}{-1}\}$ respectively and fine tune λ'_{ori}. The quantitative results in Fig. 14 (right) suggest that the best accuracy is obtained at $\lambda'_{\text{ori}} = 5\text{e}{-3}$. In summary, the optimal setting (for the 20 randomly subsampled TOSCA pairs) is $\lambda_{\text{rec}} = 3\text{e}{-1},\ \lambda'_{\text{ori}} = 5\text{e}{-3}$, which is close to the setting chosen in the main paper.